electronic materials

MDPI

Article

Determination of the Band Gap Energy of SnO_2 and ZnO Thin Films with Different Crystalline Qualities and Doping Levels

Cecilia Guillén

Centro de Investigaciones Energéticas Medioambientales y Tecnológicas (CIEMAT), Avda. Complutense 40, 28040 Madrid, Spain; c.guillen@ciemat.es

Abstract: This research is on the structural, optical, and electrical properties of SnO_2 and ZnO thin films, which are increasingly used in many electronic devices, including gas sensors, light-emitting diodes, and solar cells. For the various applications, it is essential to accurately determine the band gap energy, as it controls the optical and electrical behavior of the material. However, there is no single method for its determination; rather, different approximations depend on the crystalline quality and the doping level because these modify the energy band structure of the semiconductor. With the aim of analyzing the various approaches, SnO_2 and ZnO films were prepared by sputtering on unheated glass substrates and subsequently annealed in N_2 at various temperatures between 250 °C and 450 °C. These samples showed different crystallite sizes, absorption coefficients, and free carrier concentrations depending on the material and the annealing temperature. Analysis of the results shows that the expression developed for amorphous materials underestimates the band gap value, and the so-called unified method tends to overestimate it, while the equations for perfect or heavily doped crystals give band gap energies more consistent with the doping level, regardless of the crystalline quality of the films.

Keywords: metal oxides; thin films; crystallinity; optical absorption; carrier concentration

check for updates

Academic Editor: Wojciech Pisula

Received: 11 December 2024
Revised: 20 January 2025
Accepted: 13 February 2025
Published: 20 February 2025

Citation: Guillén, C. Determination of the Band Gap Energy of SnO_2 and ZnO Thin Films with Different Crystalline Qualities and Doping Levels. *Electron. Mater.* **2025**, *6*, 3. https://doi.org/10.3390/electronicmat6010003

Copyright: © 2025 by the author. Licensee MDPI, Basel, Switzerland. This article is an open access article distributed under the terms and conditions of the Creative Commons Attribution (CC BY) license (https://creativecommons.org/licenses/by/4.0/).

1. Introduction

SnO_2 and ZnO are n-type semiconductors based on abundant and environmentally friendly elements, which are increasingly used as active components in various fields, including gas sensors [1], light-emitting diodes [2], and solar cells [3]. Their intrinsic n-type conductivity is related to a low formation energy for metal interstitials (Zn_i, Sn_i) and oxygen vacancies (V_O) acting as donor defects [4,5]. Furthermore, extrinsic doping can be achieved by introducing substitutional donors with pentavalent cations (Sb_{Sn}, Bi_{Sn}) in SnO_2 [6,7] and with trivalent cations (Al_{Zn}, Ga_{Zn}, In_{Zn}) in ZnO [8,9], or also acceptor species such as nitrogen [10,11]. These heavily doped metal oxides (with intrinsic and/or extrinsic defects) are commonly used as transparent and conductive electrodes, which are passive components in several optoelectronic devices [12].

For the various applications of SnO_2 and ZnO, it is essential to accurately determine the band gap energy (E_g), as it controls the optical and electrical behavior of the material [13,14]. In long-range ordered solids, when the periodic potential results in sharp-edged energy bands, E_g is the minimum energy required for an electron to break free from its bound state in the valence band (VB) through promotion to an unoccupied state in the conduction band (CB), where it can participate in conduction. However, in amorphous and polycrystalline semiconductors, the structural disorder is followed by statistically varying potentials, which results in the broadening of the band edges into tails constituted by localized defect

states [15]. The existence of these localized states near the VB and the CB must be taken into account to determine E_g because it concerns the main optical transition between extended states.

Apart from band tail effects, the optical activation energy corresponds to E_g only for intrinsic or lightly doped semiconductors when the Fermi level (i.e., the E_F value that has a 50% probability of being occupied at thermodynamic equilibrium) lies within the band gap [16]. However, when the doping is increased, the Fermi level can move into the CB (n-type) or the VB (p-type), and then the optical activation energy can be higher than the band-to-band energy [12,16]. The stoichiometric changes induced by doping are also reflected as deformations of the band structure. In heavily doped semiconductors, a large number of local levels interact to form an additional band that merges with the CB (n-type) or the VB (p-type). In the case of n-type doping, the conduction electrons, together with the donor electrons, form an interacting Fermi gas that produces a distortion of the density of states and can shift the CB toward the VB [17].

Several methods have been used to obtain the absorption coefficient of semiconductors by optical spectroscopy from the measured transmittance [7–9], the reflectance [13,14], or by relating both transmittance and reflectance spectra [6,18]. Furthermore, the determination of E_g from the absorption coefficient is based on different expressions, which were developed for ideal crystalline materials [19] or taking into account deformations of the band structure in amorphous [20] or heavily doped semiconductors [21]. However, due to real materials combining a number of particularities, such as distinctive crystalline qualities and doping levels in practice, it is difficult to know which expression is best to use to determine E_g. In this regard, it is worth noting that it has recently been proposed to use a unified method to obtain the "optical gap" in different materials or in materials with different deposition procedures [22] since the onset of absorption is often more relevant to the application than the detailed nature of the optical transitions.

In this work, SnO_2 and ZnO thin films were prepared by sputtering on unheated glass substrates and subsequently annealed in N_2 at various temperatures between 250 °C and 450 °C. Structural, optical, and electrical characterization of these samples showed that different crystallite sizes, absorption coefficients, and free carrier concentrations were obtained depending on the material and the annealing temperature. The discussion compares the band gap energy obtained by traditional approaches used for crystalline, amorphous, or heavily doped semiconductors, as well as the value calculated by the aforementioned unified method. The different assumptions and the corresponding equations are presented in each subsection before the analysis of results. The objective is to investigate the conceptual and numerical differences between the various approaches and the influence of the crystalline quality and the doping level on the results obtained for the band gap energy of these metal oxides. The analysis shows that the expression established for amorphous materials underestimates the band gap energy of direct transition semiconductors, and the unified method may overestimate it, while the equations for perfect or heavily doped crystals give band gap energies more consistent with the carrier concentration, regardless of the mean crystallite size of the samples.

2. Materials and Methods

Metal oxide thin films were prepared by DC magnetron sputtering in a vacuum chamber. The targets consist of 15 cm diameter disks made of pure Sn (99.99% purity) and mixed ZnO:Al_2O_3 (98:2 wt.%, 99.995% purity) for the deposition of SnO_2 and ZnO layers. The substrates are 2 mm thick soda lime glasses, which were degreased in a dilute detergent solution, rinsed in deionized water, and blown dry in N_2 gas before they were placed in front of the target. High-purity Ar and O_2 were introduced through independent

mass flow controllers after the vacuum chamber was evacuated below 1×10^{-4} Pa. The process total pressure was kept at 4×10^{-1} Pa and the sputtering power at 2 W/cm^2, adjusting the deposition time to obtain 0.3 μm film thickness. The preparation conditions were optimized for each material in previous works [6,23], using Raman spectroscopy to demonstrate the effects of intrinsic and extrinsic doping on the microstructure, which has allowed for achieving high transparency and electrical conductivity in the as-grown samples. Post-deposition annealing was carried out in a tubular furnace at temperatures of 250–450 °C for 20 min in flowing N_2. These thermal treatments have been used to improve crystallinity and modify the carrier concentration by oxygen chemisorption or desorption processes that depend on the heating temperature and the surrounding atmosphere [24].

Crystallographic properties were examined by X-ray diffraction (XRD) with a Panalytical X'Pert instrument, using the nickel-filtered Kα1 emission line of copper (λ = 1.5405 Å) in Bragg-Brentano (θ–2θ) configuration. The recorded diffraction peaks were compared to the standard powder diffraction files (PDF). The degree of crystallinity has been evaluated according to Scherrer's formula [25], which indicates that for nanostructured materials, the full width at half maximum (FWHM) of a diffraction peak is inversely proportional to the average crystallite size. The free carrier concentration of the different samples was determined with an ECOPIA Hall Measurement System. Optical measurements of the as-grown and heated films were performed with unpolarized light at normal incidence in the wavelength range from 250 to 1500 nm, using a double beam spectrophotometer Perkin-Elmer Lambda 9 equipped with an integrating sphere.

3. Results and Discussion

3.1. Crystalline Quality and Doping Level

The evolution of the XRD patterns with the heating temperature is illustrated in Figure 1, where it can be seen that the crystallization of tetragonal SnO_2 is evident only after heat treatment at 450 °C, while hexagonal crystalline ZnO is achieved in all cases, even for the unheated sample. The main diffraction peak corresponds to the (110) lattice plane for SnO_2 and to the (002) plane for ZnO, as reported for other sputtered layers [26,27]. These diffraction peaks have been used to determine the average crystallite sizes (D) that are detailed in Table 1, which includes the respective free carrier concentration (n_e) obtained by electrical measurements. An increase in the crystallite size with heating temperature is achieved for the ZnO films, going from D = 25 nm for the as-grown sample to D = 30 nm after treatment at 450 °C. A smaller size (D = 6 nm) is obtained for the SnO_2 layer heated at 450 °C, and the absence of diffraction peaks for the rest indicates values of D < 2 nm because the applicability limit of the Scherrer formula in nanostructured materials is established at 2 nm $\leq$ D $\leq$ 600 nm [25]. In this regard, it should be noted that the crystallinity of sputtered metal oxides is favored when a ceramic crystalline target is used [26,28], which applies here only to the case of ZnO.

According to Table 1, the free carrier concentration increases with heating up to T ~ 350 °C and then decreases at higher temperatures. This is related to a critical point around 350 °C where oxygen desorption processes creating V_O donors switch to oxygen adsorption and V_O extinction [29]. Compared to analogous thermal treatments performed in the air [6,24], Vo extinction is minimized in the flowing N_2 atmosphere but not completely prevented [24]. The maximum carrier concentration is higher for ZnO ($n_e = 4.2 \times 10^{20}$ cm^{-3}) than for SnO_2 ($n_e = 2.5 \times 10^{20}$ cm^{-3}), as expected due to the addition of extrinsic doping (Al_{Zn} defects) in the former case. However, after heating at 450 °C, the value decreases more for ZnO ($n_e = 1.9 \times 10^{20}$ cm^{-3}) than for SnO_2 ($n_e = 2.2 \times 10^{20}$ cm^{-3}), indicating a higher sensitivity of ZnO to oxygen adsorption. On the other hand, no significant influence of the average crystallite size on the carrier density has been found in the present experimental

conditions, and this means that the creation/extinction of donor defects is not directly related to the crystalline quality [30].

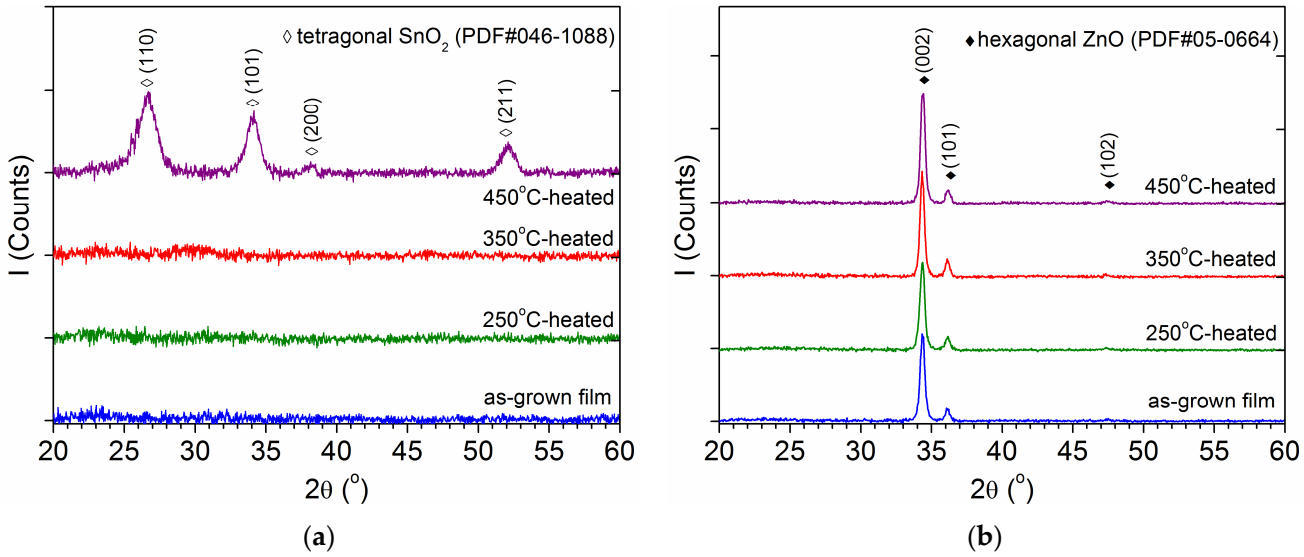

Figure 1. XRD patterns corresponding to the as-grown and heating conditions for the two different sputtered metal oxides identified as: (**a**) SnO_2 and (**b**) ZnO.

Table 1. The full width at half maximum (FWHM), the average crystallite size (D), and free carrier concentration (n_e) correspond to the SnO_2 and ZnO films as-grown and after heating.

Compound	T (°C)	FWHM (°)	D (nm)	n_e (cm^{-3})
SnO_2	As-grown	>4.25	<2	5.2×10^{18}
	250	>4.25	<2	5.1×10^{19}
	300	>4.25	<2	9.6×10^{19}
	350	>4.25	<2	2.5×10^{20}
	400	>4.25	<2	2.4×10^{20}
	450	1.305	6	2.2×10^{20}
ZnO	As-grown	0.348	25	2.4×10^{20}
	250	0.334	26	4.0×10^{20}
	300	0.312	28	4.2×10^{20}
	350	0.314	27	3.9×10^{20}
	400	0.306	28	2.4×10^{20}
	450	0.291	30	1.9×10^{20}

3.2. Absorption Coefficient Obtained from Optical Measurements

Optical measurements of transmittance (T) and/or reflectance (R) are commonly used to calculate the optical absorption coefficient (α), which defines the extinction or attenuation of light through a material [7,13,21]. However, several equations have been found to obtain α, which are based on different approximations and can be more or less accurate depending on the specific case being analyzed [18,22]. Figure 2 shows the transmittance and reflectance data recorded as a function of light wavelength for the SnO_2 and ZnO samples, as-grown and after heating. These spectra have been used to calculate the absorption coefficient following the different approximations detailed below.

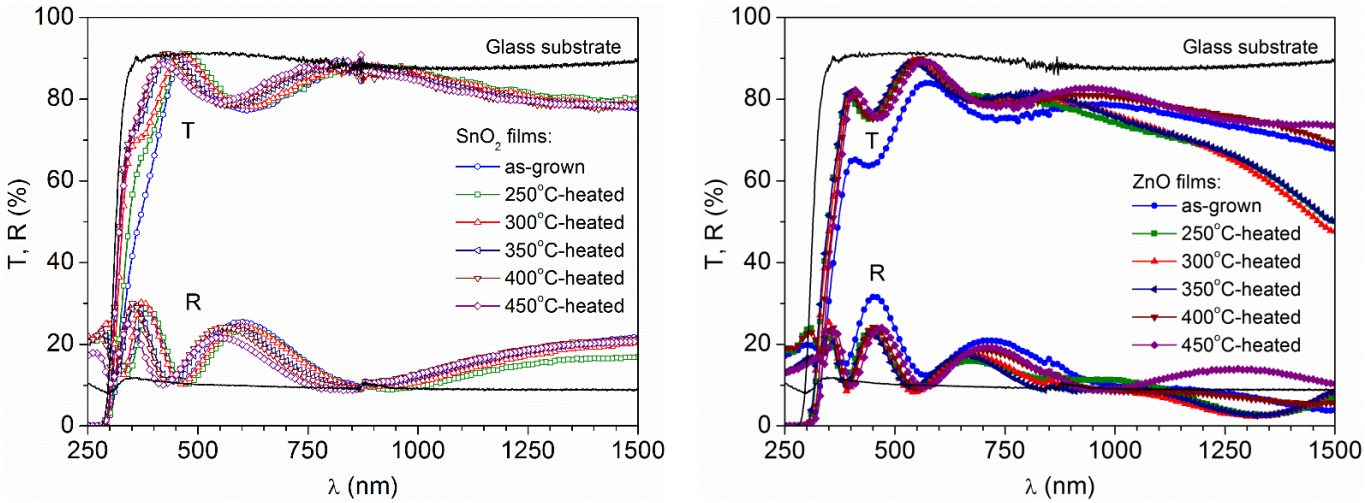

Figure 2. Transmittance and reflectance spectra corresponding to the as-grown and heating conditions for the two sputtered metal oxides: (**a**) SnO_2 and (**b**) ZnO. Spectra for a bare glass substrate are included for comparison.

The first empirical equation, which relates the absorption coefficient to the inverse of the transmittance, is the Bouguer-Beer-Lambert absorption law [31]:

$$\alpha_{BBL}(E) = \frac{1}{t}\ln\left[\frac{1}{T}\right] \quad (1)$$

where t is the material thickness or optical path length. If reflectance is also measured, this can be included by assuming that light enters the material through the first reflective interface, giving a simple optical absorption coefficient [18]:

$$\alpha_1(E) = \frac{1}{t}\ln\left[\frac{(1-R)}{T}\right]. \quad (2)$$

Further improvement can be achieved by considering that light also passes through the second reflective interface and then $(1-R)^2\exp(-\alpha t)$ exits the sample, corresponding to the transmitted radiation flux T when the product αt is large [22]:

$$\alpha_2(E) = \frac{1}{t}\ln\left[\frac{(1-R)^2}{T}\right]. \quad (3)$$

On the other hand, if αt is small, multiple internal reflections must be considered, and the whole optical absorption coefficient is given by [32]:

$$\alpha_3(E) = \frac{1}{t}\ln\left[\frac{(1-R)^2}{2T} + \sqrt{\frac{(1-R)^4}{4T^2} + R^2}\right]. \quad (4)$$

Figure 3 shows the values obtained for the absorption coefficient as a function of light energy ($E = hc/\lambda$), according to the equations expressed for α_1, α_2, and α_3. The T and R spectra corresponding to the as-grown SnO_2 and ZnO films in Figure 2 have been used for these calculations. The different approximations give analogous absorption values in the high energy (or short wavelength) region, where both T and R are small (below 30%) and, therefore, α is large (above 10^4 cm^{-1}). However, in the low energy (or long wavelength) region, where T increases greatly, it is observed that $\alpha_1 >> \alpha_3 > \alpha_2$ for both materials. This

illustrates how certain approximations can overestimate or underestimate the absorption in the low energy range, significantly affecting the subsequent determination of the band gap energy. From here on, the values given by Equation (4) will be used (i.e., $\alpha = \alpha_3$), which is the most precise because it takes into account multiple reflections in these highly transparent samples.

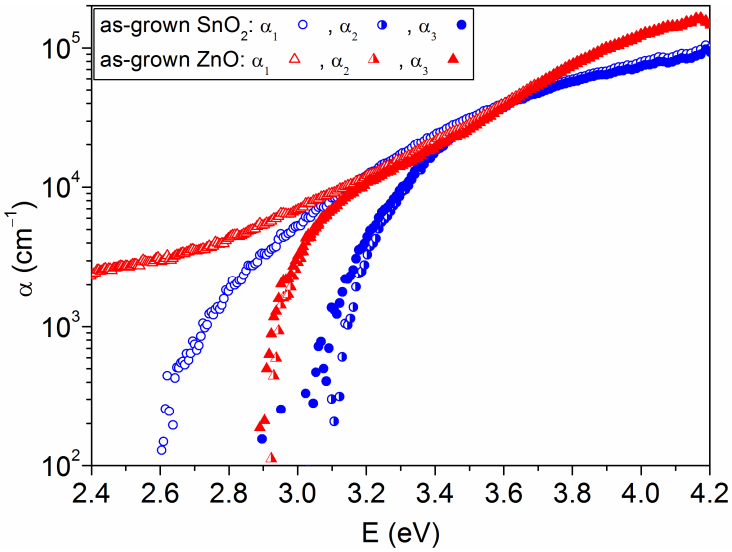

Figure 3. Comparison of the optical absorption coefficient obtained for the as-grown SnO_2 and ZnO films by applying the different approximations (α_1, α_2, and α_3) described in the main text.

3.3. Band Gap Energy in Crystalline or Amorphous Semiconductors

In the semiclassical model for crystalline semiconductors, the optical absorption at photon energy E is related to the transition rate of electrons being excited from the valence band to the conduction band [22]:

$$W_{VB\rightarrow CB} = \frac{2\pi}{h}|M|^2 N(E) \tag{5}$$

where M represents the transition matrix element and N(E) is the density of states. For ideal semiconductors with a direct optical transition, where the electron wave vector (k) remains invariant as is the case for bulk crystalline SnO_2 and ZnO [33], the relation between the band gap energy and the absorption coefficient is as follows [34]:

$$\alpha_{dir}(E) = \begin{cases} 0, & E < E_{dir} \\ A(E - E_{dir})^{1/2}, & E \geq E_{dir} \end{cases} \tag{6}$$

where A is a generic proportional constant. Therefore, E_{dir} can be determined from the least-squares linear fit of α^2 versus E, which is optimal for perfect crystals having the energy bands illustrated in Figure 4a.

For semiconductors with structural disorder, some localized states appear in the band tails depicted in Figure 4b, and even defect states can localize within the band gap, as shown in Figure 4c. Due to the presence of tail states near the VB and CB, the band gap of amorphous semiconductors is defined by the extrapolation of the joint density of states. Accordingly, Tauc et al. [20] proposed the expression:

$$\alpha_{Tauc}(E) \propto \frac{1}{E}(E - E_{Tauc})^2 \tag{7}$$

from which the band gap of any amorphous semiconductor, E_{Tauc}, can be obtained from the plot of $(E\alpha)^{1/2}$ versus E. The Tauc method has also been widely applied to polycrystalline and/or heavily doped semiconductors [16,19], although it assumes that transitions need not conserve momentum, and this cannot be ensured in a polycrystalline semiconductor with a direct band gap. Alternatively, the band gap of amorphous semiconductors has been estimated by taking the photon energy at which the optical absorption coefficient reaches 10^3 cm^{-1}, giving the so-called isoabsorption energy E_{03}, which is often close to the E_{Tauc} value [15,35].

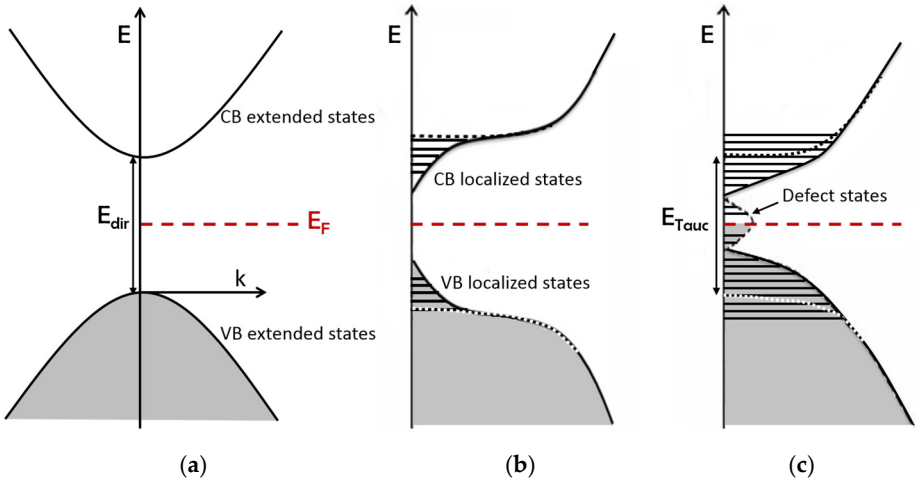

Figure 4. Illustration of energy bands for (**a**) perfect crystals with only extended states and direct band gap E_{dir}, (**b**) disordered crystals with some localized states in band tails, and (**c**) amorphous semiconductors with abundant defects and Tauc energy E_{Tauc}. Shading represents occupied states. Adapted from [15,19,22].

Equations (6) and (7) have been applied to the optical absorption data, as shown for the SnO_2 films in Figure 5a and for the ZnO layers in Figure 5b. The linear fit of α^2 vs. E gives values in the range E_{dir} = 3.47–3.96 eV for SnO_2 and E_{dir} = 3.60–3.81 eV for ZnO, while the linear fit of $(E\alpha)^{1/2}$ vs. E results in E_{Tauc} = 3.00–3.63 eV for SnO_2 and E_{Tauc} = 3.14–3.34 eV for ZnO, as summarized in Table 2. Due to the band gap widening observed for SnO_2 above 300 °C, the linear fit to obtain E_{dir} is based on fewer points, with regression coefficients ($R^2 \sim 0.85$) somewhat lower than for the rest ($R^2 > 0.95$). For each sample, $E_{dir} > E_{Tauc}$ because the corresponding plots highlight the optical absorption occurring in different energy regions (high or low, respectively). Here, the same relationship $(E_{dir} - E_{Tauc}) = (0.45 \pm 0.05)$ eV is observed for both materials, although the crystallite size changes. In fact, a comparison of the data in Tables 1 and 2 indicates that the free carrier concentration plays a more important role than the crystallite size in determining the band gap energy of these materials, as discussed in Section 3.5. The direct band gap energies for bulk crystalline SnO_2 and ZnO are 3.6 eV and 3.4 eV, respectively [33]. For polycrystalline films, the structural disorder can give somewhat lower direct gap energies, typically above 3.4 eV for SnO_2 [36,37] and above 3.3 eV for ZnO [38,39], while the increase in carrier concentration can result in transition energies above that of the bulk crystalline semiconductor [39]. Otherwise, Tauc energies below 3.0 eV are reported for amorphous SnO_2 [40,41]. Therefore, the results shown in Figure 5 are in agreement with the literature.

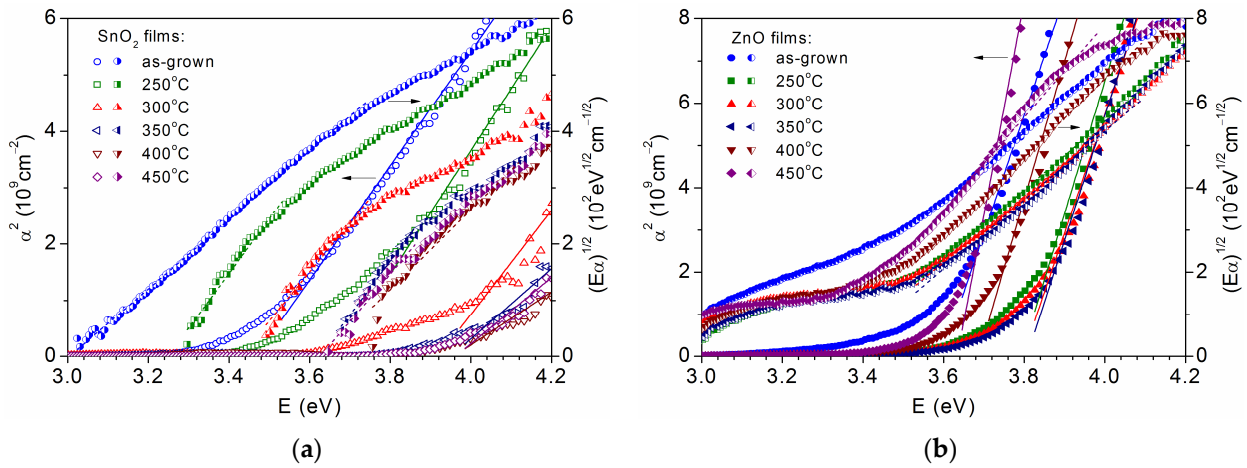

Figure 5. Plots of α^2 and $(E\alpha)^{1/2}$ as a function of photon energy E, corresponding to the as-grown and heating conditions for the two sputtered metal oxides: (**a**) SnO_2; (**b**) ZnO.

Table 2. Band gap energies obtained from the plots in Figure 5 for the SnO_2 and ZnO films as-grown and after heating.

Compound	T (°C)	E_{dir} (eV)	E_{Tauc} (eV)
SnO_2	As-grown	3.47	3.00
	250	3.67	3.25
	300	3.90	3.43
	350	3.95	3.62
	400	3.96	3.63
	450	3.96	3.63
ZnO	As-grown	3.60	3.14
	250	3.79	3.31
	300	3.80	3.31
	350	3.81	3.34
	400	3.69	3.29
	450	3.63	3.28

3.4. Band Gap Energy in Heavily Doped Semiconductors and Unified Method

The analysis of heavily doped semiconductors requires some additional considerations. In degenerate n-type doping, the Fermi level moves into the CB, and the height of the Fermi level above the CB minimum increases with increasing carrier concentration [42]. Therefore, optical transitions from the VB top to states at the CB bottom are no longer possible, and only energetically higher states in the CB can be occupied, as illustrated in Figure 6. This broadening of the optical gap due to filled CB states (equally for p-type doping with hole-filled VB states) is called the Burstein–Moss (BM) shift or ΔE_{BM} [30]. As the free carrier concentration increases, the BM shift is counteracted by the band gap renormalization (BGR) effect, which is a band gap narrowing caused by the correlated motion of free carriers and their scattering against ionized defects [42], being difficult to unravel the impact of doping on these phenomena [43]. Analysis of experimental data using a time-dependent perturbation theory for the transition rate has shown [21] that the

absorption coefficient of heavily doped semiconductors is well-fitted by a Lorentzian-type broadening function:

$$\alpha_{dop}(E) \propto (\Delta E_{BM})^{\frac{1}{2}} \left[1 - \frac{2}{\pi}\tan^{-1}\left\{\frac{W + \Delta E_{BM} - E}{\Gamma}\right\}\right]. \quad (8)$$

where Γ is a frequency-independent broadening parameter, and W is the minimum energy distance between CB and VB. The inflection point obtained from the α versus E plot (i.e., the maximum point of dα/dE) gives the transition energy $E_{dop} = W + \Delta E_{BM}$ for these materials [21,39].

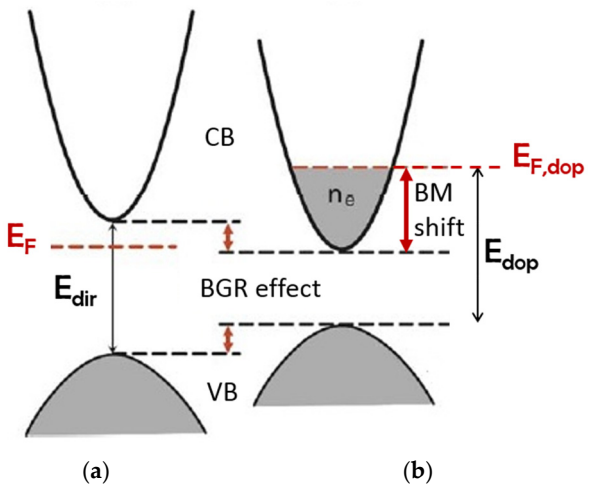

Figure 6. Illustration of changes in the energy bands from (**a**) lightly doped crystals with direct band gap energy E_{dir} to (**b**) heavily doped crystals with transition energy E_{dop} due to the band gap renormalization (BGR) effect and the Burstein–Moss (BM) shift when the carrier concentration (n_e) increases. Shading represents occupied states. Adapted from [21,38,42].

In recent years, a unified methodology has been proposed to determine the band gap energy, which is based on the fitting of the absorption spectrum according to the sigmoid-Boltzmann function [22]:

$$\alpha_{Boltz}(E) = \alpha_{max} + \frac{\alpha_{min} - \alpha_{max}}{1 + \exp\left(\frac{E - E_{0,Boltz}}{\delta E}\right)} \quad (9)$$

where α_{min} (α_{max}) represents the minimum (maximum) absorption coefficient, $E_{0,Boltz}$ is the energy coordinate at which the absorption coefficient is halfway between α_{min} and α_{max}, and δE is associated with the slope of the sigmoid curve. After applying Equation (9) to various semiconductors in crystalline and amorphous forms, an empirical relationship has been established to obtain the band gap energy as follows [22]:

$$E_{Bolz} = E_{0,Boltz} - n_{dir/ind}\delta E, \quad (10)$$

with a factor $n_{dir} \sim 0.3$ and $n_{ind} \sim 4.3$ for direct and indirect band gap materials, respectively. According to this scheme, direct gaps are defined by optical transitions taking place near the high absorption edge, and indirect gaps are defined by optical transitions around the absorption onset region. Furthermore, the value of the slope δE indicates the energy extent over which most optical transitions occur, which will increase with the structural-electronic disorder of the semiconductor.

The application of Equations (8)–(10) to the present absorption data is shown for the SnO_2 layers in Figure 7a and for the ZnO films in Figure 8a. The maximum point

of the differential function ($d\alpha/dE$) is used to obtain E_{dop} = 3.47–4.02 eV for SnO_2 and E_{dop} = 3.58–3.76 eV for ZnO, while the fit to the Boltzmann function results in E_{Boltz} = 3.61–3.96 eV for SnO_2 and E_{Boltz} = 3.73–4.04 eV for ZnO, taking the factor n_{dir} = 0.3 for both materials. A good agreement between the values of E_{dop} and E_{dir} is observed, being $E_{dop} = (E_{dir} \pm 0.05)$ eV for the different samples. Otherwise, E_{Boltz} tends to be higher than E_{dop} or E_{dir} because the empirical factor (n_{dir} = 0.3) is designed to approximate E_{Boltz} to the band gap of the respective bulk crystal, even for highly disordered structures with low carrier concentrations [22]. The value of the slope in Figure 7b is in the range δE = 0.3–0.5 for the SnO_2 samples heated to T ≤ 300 °C and then decreases for higher temperatures to a minimum δE = 0.14 at T = 450 °C, which corresponds to SnO_2 with a crystallite size D = 6 nm. On the other hand, the slope in Figure 8b is in the range δE = 0.19–0.11 for the ZnO films with D = 25–30 nm. Therefore, the δE factor is actually larger for amorphous layers (D < 2 nm) but is not useful for distinguishing between different crystallite sizes in the range D = 6–30 nm. This indicates that the electronic disorder is not only related to crystalline quality but there may also be amorphous layers with electronic band structures similar to polycrystalline films.

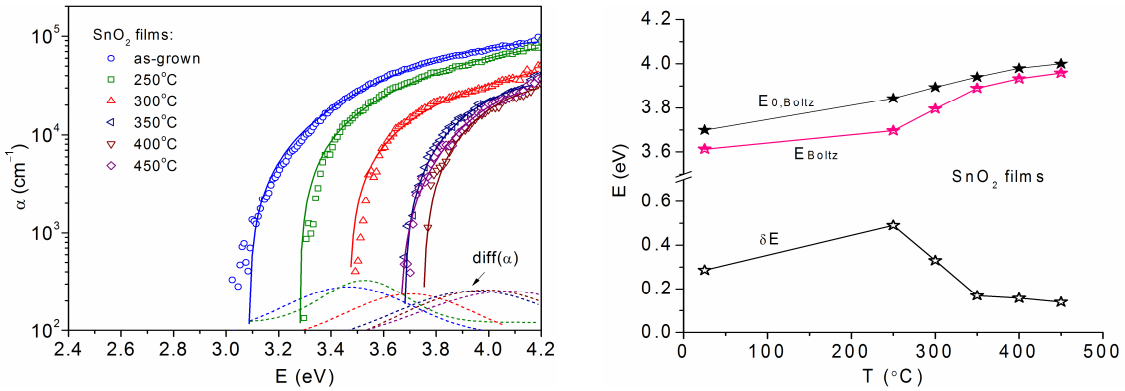

(**a**) (**b**)

Figure 7. (**a**) Optical absorption coefficients as a function of photon energy for the as-grown and heated SnO_2 films. The dashed lines represent the differential function ($d\alpha/dE$) used to obtain E_{dop} and the solid lines the fit to the Boltzmann function; (**b**) evolution of the values of $E_{0,Boltz}$, δE, and E_{Boltz} with heating temperature.

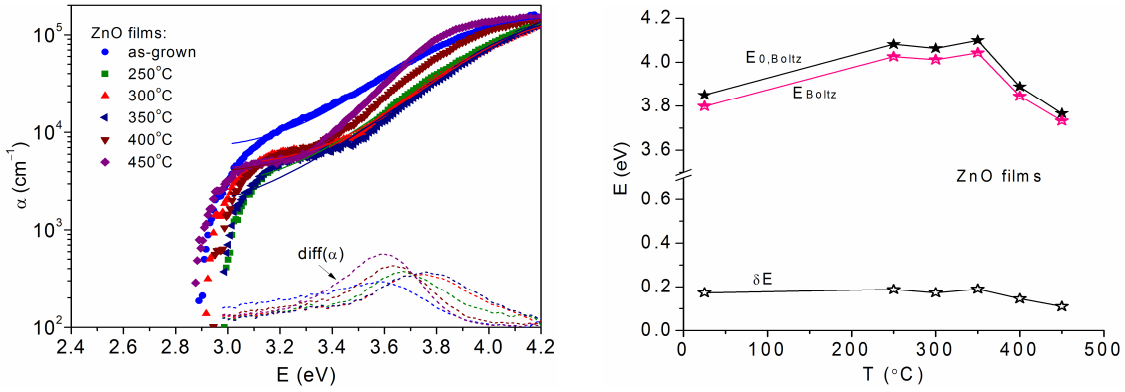

(**a**) (**b**)

Figure 8. (**a**) Optical absorption coefficients as a function of photon energy for the as-grown and heated ZnO films. The dashed lines represent the differential function ($d\alpha/dE$) used to obtain E_{dop} and the solid lines the fit to the Boltzmann function; (**b**) evolution of the values of $E_{0,Boltz}$, δE, and E_{Boltz} with heating temperature.

3.5. Comparison of Band Gap Values for Different Doping Levels

The gap values obtained in the previous subsections (E_{dir}, E_{Tauc}, E_{dop}, and E_{Boltz}) are plotted as a function of the respective carrier concentration for the SnO_2 films in Figure 9 and for the ZnO layers in Figure 10. The evolution of these data will now be analyzed according to the gap widening due to the Burstein–Moss shift, which can be expressed by [44]:

$$\Delta E_{BM} = \frac{\hbar^2}{2m_e^*}\left(3\pi^2 n_e\right)^{2/3}, \tag{11}$$

where $\hbar$ is the reduced Planck's constant ($\hbar$ = 6.582 × 10^{-16} eVs), n_e is the free electron concentration, and m_e^* is the conductivity effective mass, being $m_e^* = 0.3\ m_e$ for the lightly doped materials [41,45], with m_e the electron rest mass (m_e = 5.110 × 10^5 eV/c^2). For heavily doped metal oxides, a higher effective mass ($m_e^* = 0.5\ m_e$) has been reported [46] due to nonparabolicity effects when the optical transition occurs in a band located far from the CB bottom. Moreover, the lowering of electron energies due to many-body interactions produces a gap narrowing, the band gap renormalization illustrated in Figure 6. Although the ion-carrier correlation, as well as the minority carrier correlation, might play a significant role in the renormalization [47], here, the electron-donor and electron-hole interactions can be neglected because the number of generated electrons is much larger than the number of holes and donors in the annealed samples [48]. Therefore, only the electron-electron interactions are considered, which can be estimated using a weakly interacting electron gas model as follows [39]:

$$\Delta E_{BGR} = \frac{e^2}{2\pi\varepsilon_S\varepsilon_0}\left(\frac{3n_e}{\pi}\right)^{1/3} \tag{12}$$

where ε_S is the static relative permittivity, taking here ε_S = 3.5 [45], and ε_0 is the vacuum permittivity: ε_0 = 5.526 × 10^7 e^2/(eV m). Then, the gap energy of these heavily doped semiconductors is expected to change with respect to that of the undoped material ($E_{g,0}$) according to the expression:

$$E_{g,dop} = E_{g,0} + \Delta E_{BM} - \Delta E_{BGR} \tag{13}$$

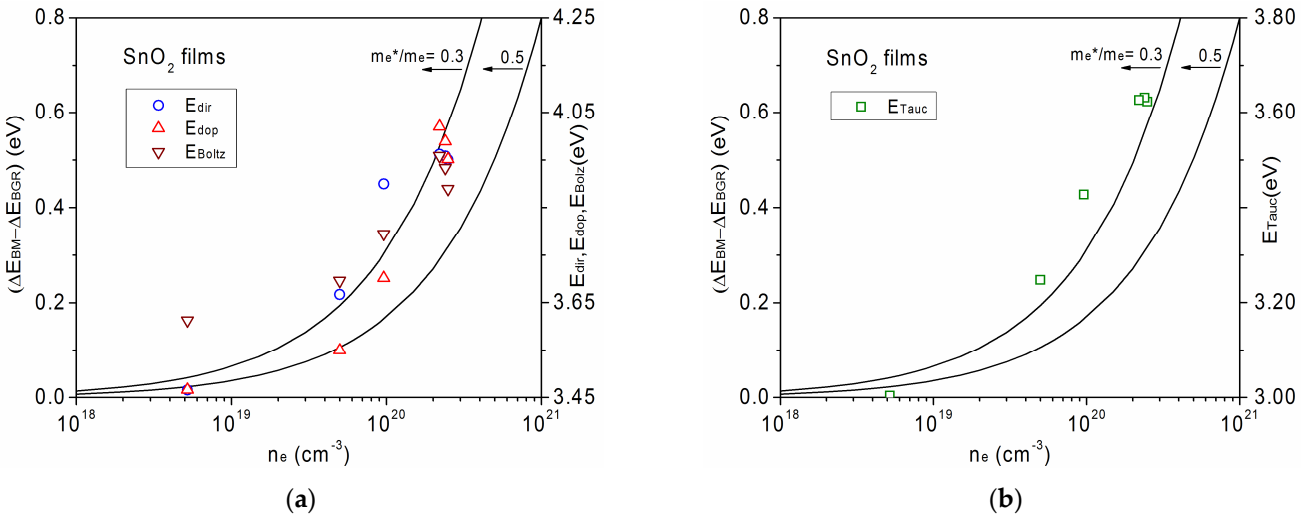

Figure 9. Evolution of the energy gap with carrier concentration (n_e) obtained for SnO_2 from the different approximations: (**a**) E_{dir}, E_{dop}, E_{Boltz}; (**b**) E_{Tauc}. The solid lines represent the expected change ($\Delta E_{BM} - \Delta E_{BGR}$) for two different effective mass values.

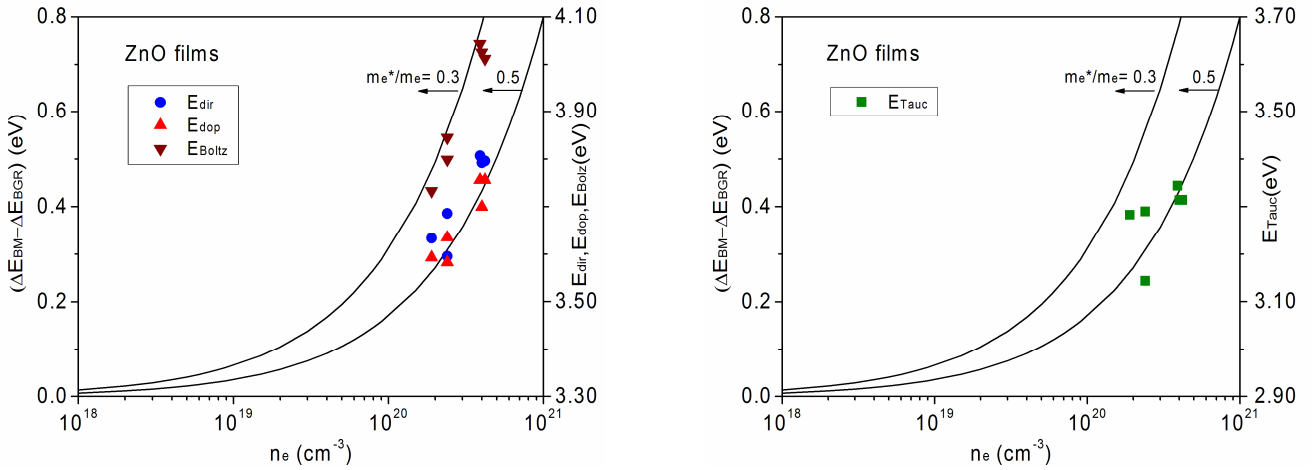

Figure 10. Evolution of the energy gap with carrier concentration (n_e) obtained for ZnO from the different approximations: (**a**) E_{dir}, E_{dop}, E_{Boltz}; (**b**) E_{Tauc}. The solid lines represent the expected change ($\Delta E_{BM} - \Delta E_{BGR}$) for two different effective mass values.

Equations (11) and (12) have been used to calculate the variation of ($\Delta E_{BM} - \Delta E_{BGR}$) as a function of the carrier concentration for two different effective mass values, $m_e^*/m_e = 0.3$ and $m_e^*/m_e = 0.5$. Figure 9 shows a good fit of the SnO_2 experimental data to the function with $m_e^*/m_e = 0.3$, considering the undoped gap energy results in $E_{g,0}$ = 3.00 eV with the E_{Tauc} data and $E_{g,0}$ = 3.45 eV for the rest. On the other hand, the ZnO samples represented in Figure 10 give a good agreement with $m_e^*/m_e = 0.3$ for the E_{Boltz} values, but a better fit to $m_e^*/m_e = 0.5$ for all others, being now $E_{g,0}$ = 2.90 eV for the E_{Tauc} data and $E_{g,0}$ = 3.30 eV for the rest. At this point, it is worth noting that all approximations are useful for evaluating the variation of the optical transition with the doping level, according to BM and BGR effects. However, the Tauc equation underestimates the undoped gap since all the others coincide on a larger $E_{g,0}$, which is in better agreement with that reported for SnO_2 [37] and ZnO [38] thin films. Otherwise, the unified method tends to overestimate the transition energy at low carrier concentrations due to the attempt to bring E_{Bolz} closer to the bulk crystalline gap value (Figure 9a) and sometimes at high carrier densities due to the assumption of parabolic edges (Figure 10a). In conclusion, E_{dir} and E_{dop} are found to be equivalent and more suitable for determining the gap energy at different carrier concentrations, allowing the assessment of non-parabolicity effects.

4. Conclusions

Reactive sputtering of pure Sn and mixed ZnO:Al_2O_3 targets onto unheated glass substrates results in metal oxide films with different crystallite sizes (D) and free carrier concentrations (n_e), being D < 2 nm and $n_e = 5.2 \times 10^{18}$ cm^{-3} for the SnO_2 layers, and D = 25 nm and $n_e = 2.4 \times 10^{20}$ cm^{-3} for the ZnO samples. Subsequent heating in flowing N_2 increases the carrier density to a maximum of $n_e = 2.5 \times 10^{20}$ cm^{-3} for SnO_2 and $n_e = 4.2 \times 10^{20}$ cm^{-3} for ZnO, which is reached around 350 °C, where oxygen desorption processes creating V_O donors switch to oxygen adsorption and V_O extinction. Otherwise, the maximum crystallite size, D = 6 nm for SnO_2 and D = 30 nm for ZnO, is obtained by heating to 450 °C.

For each sample, the band gap energy has been calculated by different equations, which were established for crystalline, amorphous or heavily doped semiconductors. Comparative analysis indicates that all approximations are useful to evaluate the variation of the optical transition with n_e, in good agreement with the Burstein–Moss (BM) shift

and band gap renormalization (BGR) effects, while the crystalline quality is not a decisive factor to explain the optical behavior of these films. Nevertheless, the Tauc equation, which was developed for amorphous semiconductors, underestimates the undoped direct band gap ($E_{g,0}$) by focusing on the absorption onset rather than on higher absorption ranges. Otherwise, the so-called unified method tends to overestimate the transition energy ($E_{g,dop} = E_{g,0} + \Delta E_{BM} - \Delta E_{BGR}$) because the empirical factor and the assumption of parabolic edges are not always suitable. Finally, the values obtained supposing perfect crystalline and heavily doped semiconductors turn out to be equivalent, giving $E_{g,0}$ = 3.45 eV for SnO_2 and $E_{g,0}$ = 3.30 eV for ZnO. These methods have also allowed to assess an effective mass of $m_e^*/m_e = 0.3$ for SnO_2 and $m_e^*/m_e = 0.5$ for ZnO, the increase being related to nonparabolic edges, resulting in a smaller BM shift.

Funding: This research received no external funding.

Data Availability Statement: Data are contained within the article.

Conflicts of Interest: The author declares no conflicts of interest.

References

1. Sivaperuman, K.; Thomas, A.; Thangavel, R.; Thirumalaisamy, L.; Palanivel, S.; Pitchaimuthu, S.; Ahsan, N.; Okada, Y. Binary and ternary metal oxide semiconductor thin films for effective gas sensing applications: A comprehensive review and future prospects. *Prog. Mater. Sci.* **2024**, *142*, 101222. [CrossRef]
2. Vasanthi, V.; Sivanantham, N.; Saathvika, L.; Gopalakrishnan, N. Metal oxide charge transport materials for light emitting diodes—An overview. *Mater. Sci. Semicond. Process.* **2023**, *165*, 107679. [CrossRef]
3. Armstrong, P.J.; Chapagain, S.; Panta, R.; Grapperhaus, C.; Druffel, T. Synthesizing and formulating metal oxide nanoparticle inks for perovskite solar cells. *Chem. Commun.* **2023**, *59*, 12248–12261. [CrossRef] [PubMed]
4. Kílíç, C.; Zunger, A. Origins of coexistence of conductivity and transparency in SnO_2. *Phys. Rev. Lett.* **2002**, *88*, 95501. [CrossRef]
5. Buckeridge, J.; Catlow, C.R.A.; Farrow, M.R.; Logsdail, A.J.; Scanlon, D.O.; Keal, T.W.; Sherwood, P.; Woodley, S.M.; Sokol, A.A.; Walsh, A. Deep vs shallow nature of oxygen vacancies and consequent n-type carrier concentrations in transparent conducting oxides. *Phys. Rev. Mater.* **2018**, *2*, 56–59. [CrossRef]
6. Guillén, C.; Herrero, J. Intrinsic and extrinsic doping contributions in SnO_2 and SnO_2:Sb thin films prepared by reactive sputtering. *J. Alloys Compd.* **2019**, *791*, 68–74. [CrossRef]
7. Akkera, H.S.; Sivakumar, P.; Bitla, Y.; Vanga, G.; Kambhala, N.; Naveen, C.S.; Reddy, T.R.K.; Reddy, G.S. Structural, electrical, and optical properties of spin-coated Bi:SnO_2 transparent conducting oxide thin films. *Phys. B Condens. Matter* **2022**, *638*, 413839. [CrossRef]
8. Kumar, A.; Ahmad, M.I. Role of defects in the electronic properties of Al doped ZnO films deposited by spray pyrolysis. *J. Mater. Sci.* **2022**, *57*, 7877–7895. [CrossRef]
9. El Filali, B.; Torchynska, T.; Ballardo Rodríguez, I.C.; Douda, J.; Polupan, G. Transmittance, structure and resistivity of ZnO films doped with Ga and In elements for TCO applications. *J. Mater. Sci. Mater. Electron.* **2023**, *34*, 983. [CrossRef]
10. Xie, Y. Synthesis and electrochemical performance of an electroactive nitrogen-doping SnO_2 nanoarray supported on carbon fiber. *J. Chem. Res.* **2021**, *45*, 738–746. [CrossRef]
11. Nicolescu, M.; Anastasescu, M.; Preda, S.; Stroescu, H.; Stoica, M.; Teodorescu, V.S.; Aperathitis, E.; Kampylafka, V.; Modreanu, M.; Zaharescu, M.; et al. Influence of the substrate and nitrogen amount on the microstructural and optical properties of thin r.f.-sputtered ZnO films treated by rapid thermal annealing. *Appl. Surf. Sci.* **2012**, *261*, 815–823. [CrossRef]
12. Shi, J.; Zhang, J.; Yang, L.; Qu, M.; Qi, D.; Zhang, K.H.L. Wide bandgap oxide semiconductors: From materials physics to optoelectronic devices. *Adv. Mater.* **2021**, *33*, 2006230. [CrossRef] [PubMed]
13. Welter, E.S.; Garg, S.; Gläser, R.; Goepel, M. Methodological investigation of the band gap determination of solid semiconductors via UV/Vis spectroscopy. *ChemPhotoChem* **2023**, *7*, e202300001. [CrossRef]
14. Makuła, P.; Pacia, M.; Macyk, W. How to correctly determine the band gap energy of modified semiconductor photocatalysts based on UV–Vis spectra. *J. Phys. Chem. Lett.* **2018**, *9*, 6814–6817. [CrossRef]
15. Mullerova, J.; Sutta, P. On some ambiguities of the absorption edge and optical band gaps of amorphous and polycrystalline semiconductors. *Commun.—Sci. Lett. Univ. Zilina* **2017**, *19*, 9–15. [CrossRef]
16. Dolgonos, A.; Mason, T.O.; Poeppelmeier, K.R. Direct optical band gap measurement in polycrystalline semiconductors: A critical look at the Tauc method. *J. Solid State Chem.* **2016**, *240*, 43–48. [CrossRef]
17. Van Mieghem, P. Theory of band tails in heavily doped semiconductors. *Rev. Mod. Phys.* **1992**, *64*, 755–793. [CrossRef]

18. Hong, W.Q. Extraction of extinction coefficient of weak absorbing thin films from special absorption. *J. Phys. D Appl. Phys.* **1989**, *22*, 1384–1385. [CrossRef]
19. Klein, J.; Kampermann, L.; Mockenhaupt, B.; Behrens, M.; Strunk, J.; Bacher, G. Limitations of the Tauc plot method. *Adv. Funct. Mater.* **2023**, *33*, 2304523. [CrossRef]
20. Tauc, J.; Grigorovici, R.; Vancu, A. Optical properties and electronic structure of amorphous germanium. *Phys. Status Solidi* **1966**, *15*, 627–637. [CrossRef]
21. Hamberg, I.; Granqvist, C.G.; Berggren, K.F.; Sernelius, B.E.; Engström, L. Band-gap widening in heavily Sn-doped In_2O_3. *Phys. Rev. B* **1984**, *30*, 3240–3249. [CrossRef]
22. Zanatta, A.R. Revisiting the optical bandgap of semiconductors and the proposal of a unified methodology to its determination. *Sci. Rep.* **2019**, *9*, 11225. [CrossRef] [PubMed]
23. Guillén, C.; Herrero, J. High conductivity and transparent ZnO:Al films prepared at low temperature by DC and MF magnetron sputtering. *Thin Solid Films* **2006**, *515*, 640–643. [CrossRef]
24. Guillén, C.; Herrero, J. Comparing the plasmonic characteristics of sputtered ZnO:Al and In_2O_3:Sn thin films as a function of the heating temperature and atmosphere. *Thin Solid Films* **2016**, *605*, 136–142. [CrossRef]
25. Vorokh, A.S. Scherrer formula: Estimation of error in determining small nanoparticle size. *Nanosyst. Phys. Chem. Math.* **2018**, *9*, 364–369. [CrossRef]
26. Yang, W.; Yu, S.; Zhang, Y.; Zhang, W. Properties of Sb-doped SnO_2 transparent conductive thin films deposited by radio-frequency magnetron sputtering. *Thin Solid Films* **2013**, *542*, 285–288. [CrossRef]
27. Badgujar, A.C.; Yadav, B.S.; Jha, G.K.; Dhage, S.R. Room temperature sputtered aluminum-doped ZnO thin film transparent electrode for application in solar cells and for low-band-gap optoelectronic devices. *ACS Omega* **2022**, *7*, 14203–14210. [CrossRef]
28. Ye, W.; Fang, K. Comparative study on structure and properties of ZnO thin films prepared by RF magnetron sputtering using pure metallic Zn target and ZnO ceramic target. *Surf. Eng.* **2020**, *36*, 49–54. [CrossRef]
29. Kim, I.H.; Ko, J.H.; Kim, D.; Lee, K.S.; Lee, T.S.; Jeong, J.-H.; Cheong, B.; Baik, Y.-J.; Kim, W.M. Scattering mechanism of transparent conducting tin oxide films prepared by magnetron sputtering. *Thin Solid Films* **2006**, *515*, 2475–2480. [CrossRef]
30. Saw, K.G.; Aznan, N.M.; Yam, F.K.; Ng, S.S.; Pung, S.Y. New insights on the Burstein-Moss shift and band gap narrowing in indium-doped zinc oxide thin films. *PLoS ONE* **2015**, *10*, e0141180. [CrossRef]
31. Mayerhöfer, T.G.; Pahlow, S.; Popp, J. The Bouguer-Beer-Lambert law: Shining light on the obscure. *ChemPhysChem* **2020**, *21*, 2029–2046. [CrossRef] [PubMed]
32. Kushnir, O.S. Effect of multiple reflections of light on the optical characteristics of crystals. *J. Opt. A Pure Appl. Opt.* **2003**, *5*, 478–488. [CrossRef]
33. Ellmer, K. Resistivity of polycrystalline zinc oxide films: Current status and physical limit. *J. Phys. D Appl. Phys.* **2001**, *34*, 3097–3108. [CrossRef]
34. Rosencher, E.; Vinter, B. *Optoelectronics*; Cambridge University Press: Cambridge, UK, 2002; ISBN 9780521771290.
35. Ruiz-Pérez, J.J.; Navarro, E.M. Optical transmittance for strongly-wedge-shaped semiconductor films: Appearance of envelope-crossover points in amorphous as-based chalcogenide materials. *Coatings* **2020**, *10*, 1063. [CrossRef]
36. Lin, S.S.; Tsai, Y.S.; Bai, K.R. Structural and physical properties of tin oxide thin films for optoelectronic applications. *Appl. Surf. Sci.* **2016**, *380*, 203–209. [CrossRef]
37. Körber, C.; Ágoston, P.; Klein, A. Surface and bulk properties of sputter deposited undoped and Sb-doped SnO_2 thin films. *Sens. Actuators B Chem.* **2009**, *139*, 665–672. [CrossRef]
38. Liu, Y.; Li, Y.; Zeng, H. ZnO-based transparent conductive thin films: Doping, performance, and processing. *J. Nanomater.* **2013**, *2013*, 196521. [CrossRef]
39. Kim, W.M.; Kim, J.S.; Jeong, J.H.; Park, J.K.; Baik, Y.J.; Seong, T.Y. Analysis of optical band-gap shift in impurity doped ZnO thin films by using nonparabolic conduction band parameters. *Thin Solid Films* **2013**, *531*, 430–435. [CrossRef]
40. Shokr, E.K.; Wakkad, M.M.; Abd El-Ghanny, H.; Ali, H.M. Sb-doping effects on optical and electrical parameters of SnO_2 films. *J. Phys. Chem. Solids* **2000**, *61*, 75–85. [CrossRef]
41. So, H.S.; Park, J.; Jung, D.H.; Ko, K.H.; Lee, H. Optical properties of amorphous and crystalline Sb-doped SnO_2 thin films studied with spectroscopic ellipsometry: Optical gap energy and effective mass. *J. Appl. Phys.* **2015**, *118*, 085303. [CrossRef]
42. Walsh, A.; Da Silva, J.L.F.; Wei, S.H. Origins of band-gap renormalization in degenerately doped semiconductors. *Phys. Rev. B—Condens. Matter Mater. Phys.* **2008**, *78*, 075211. [CrossRef]
43. Zhang, J.; Willis, J.; Yang, Z.; Sheng, Z.; Wang, L.-S.; Lee, T.-L.; Chen, L.; Scanlon, D.O.; Zhang, K.H.L. Direct determination of band-gap renormalization in degenerately doped ultrawide band gap β-Ga_2O_3 semiconductor. *Phys. Rev. B* **2022**, *106*, 205305. [CrossRef]
44. Ivchenko, V. Theory of Burstein-Moss effect in semiconductors with anisotropic energy bands. *Phys. Scr.* **2024**, *99*, 035952. [CrossRef]

45. Guillén, C.; Herrero, J. Structural and plasmonic characteristics of sputtered SnO_2:Sb and ZnO:Al thin films as a function of their thickness. *J. Mater. Sci.* **2016**, *51*, 7276–7285. [CrossRef]
46. Abdolahzadeh Ziabari, A.; Rozati, S.M. Carrier transport and bandgap shift in n-type degenerate ZnO thin films: The effect of band edge nonparabolicity. *Phys. B Condens. Matter* **2012**, *407*, 4512–4517. [CrossRef]
47. Sans, J.A.; Sánchez-Royo, J.F.; Segura, A.; Tobias, G.; Canadell, E. Chemical effects on the optical band-gap of heavily doped ZnO: MIII (M = Al, Ga, In): An investigation by means of photoelectron spectroscopy, optical measurements under pressure, and band structure calculations. *Phys. Rev. B—Condens. Matter Mater. Phys.* **2009**, *79*, 195105. [CrossRef]
48. Kim, C.E.; Moon, P.; Kim, S.; Myoung, J.M.; Jang, H.W.; Bang, J.; Yun, I. Effect of carrier concentration on optical bandgap shift in ZnO:Ga thin films. *Thin Solid Films* **2010**, *518*, 6304–6307. [CrossRef]

Disclaimer/Publisher's Note: The statements, opinions and data contained in all publications are solely those of the individual author(s) and contributor(s) and not of MDPI and/or the editor(s). MDPI and/or the editor(s) disclaim responsibility for any injury to people or property resulting from any ideas, methods, instructions or products referred to in the content.